

# Negative-quench-induced excitation dynamics of ultracold bosons in one-dimensional lattices

S.I. Mistakidis,<sup>1</sup> L. Cao,<sup>1,2</sup> and P. Schmelcher<sup>1,2</sup>

<sup>1</sup>*Zentrum für Optische Quantentechnologien, Universität Hamburg,  
Luruper Chaussee 149, 22761 Hamburg, Germany*

<sup>2</sup>*The Hamburg Centre for Ultrafast Imaging, Universität Hamburg,  
Luruper Chaussee 149, 22761 Hamburg, Germany*

(Dated: February 9, 2015)

The nonequilibrium dynamics following a quench of strongly repulsive bosonic ensembles in one-dimensional finite lattices is investigated by employing interaction quenches and/or a ramp of the lattice potential. Both sudden and time-dependent quenches are analyzed in detail. For the case of interaction quenches we address the transition from the strong repulsive to the weakly-interacting regime, suppressing in this manner the heating of the system. The excitation modes such as the cradle process and the local breathing mode are examined via local density observables. In particular, the cradle mode is inherently related to the initial delocalization and, following a negative interaction quench, can be excited only for incommensurate setups with filling larger than unity. Alternatively, a negative quench of the lattice depth which favors the spatial delocalization is used to access the cradle mode for setups with filling smaller than unity. Our results shed light on possible schemes to control the cradle and the breathing modes. Finally, employing the notion of fidelity we study the dynamical response of the system after a diabatic or adiabatic parameter modulation for short and long evolution times. The evolution of the system is obtained numerically using the ab-initio multi-layer multi-configuration time-dependent Hartree method for bosons which permits to follow non-equilibrium dynamics including the corresponding investigation of higher-band effects.

Keywords: sudden quench; time-dependent quench; interaction quench; barrier quench; non-equilibrium dynamics; controlled dynamics; higher-band effects; excitation modes; fidelity.

PACS numbers: 03.75.Lm, 67.57.Hi, 67.57.Jj, 67.85.Hj

## I. Introduction

The realization of ultracold atomic gases has opened up exciting possibilities for the study of the non-equilibrium quantum dynamics of many-body systems [1, 2]. The high degree of tunability and the good isolation from the environment renders ultracold gases a versatile tool to realize systems far from equilibrium as they remain coherent for sufficiently long time scales, allowing us to probe them experimentally [3–5]. In particular, the dynamical response of a closed quantum system can be investigated via a sudden change (i.e. a rapid perturbation compared to any other characteristic time scale of the system) of a Hamiltonian parameter called ‘quantum quench’. Typically, in such a scenario the many-body system is initially prepared in a characteristic state which is not an eigenstate of the perturbed Hamiltonian, and the subsequent time-evolution is explored. In this way, important aspects can be studied such as the connection between the final and initial states or the emergence of a steady state [6]. Despite recent theoretical advances (see Ref. [2] and references therein), our understanding of strongly correlated quantum gases after a quench is far from complete and constitutes an appealing problem of modern quantum physics [7–13].

In a previous work [14] following a sudden raise of the interparticle repulsion (positive quench) we explored the dynamics of initially weakly interacting superfluids.

As a consequence a cradle mode generated by the over-barrier transport of bosons residing in neighboring wells and caused by the import of energy to the system has been detected. This mode has further been identified as a two-body intrawell collision which was dipole-like [15, 16]. In addition, a local-breathing mode reminiscent to the usual breathing mode in a harmonic trap [17–22] has been observed. The occurrence of a resonance between a tunneling mode and the cradle giving rise to the controllability between the inter and intrawell dynamics has also been revealed. However, the above scenario can also give rise to unavoidable heating processes especially for large quench amplitudes. To overcome this ambiguity i.e. minimize the heating [23] one can start from strong interparticle repulsion and quench back to weak interactions called negative interaction quench. A negative quench may lead to a drastically different dynamical behaviour as the filling factor  $\nu$  is expected to play a crucial role. Here, an intriguing aspect would be to explore how the initial spatial configuration of the system, reflected by the corresponding filling factor, affects the system dynamics and as a consequence the generation of the emergent excited modes. This investigation will permit us to gain a deeper understanding of the on-site excited modes (especially the cradle mode), the underlying microscopic mechanisms and their controllability in terms of the tunable parameters of the Hamiltonian.

In this work a systematic ab-initio analysis of the non-equilibrium dynamics of strongly repulsive interacting

bosons in one-dimensional (1D) lattices is carried out. To this end, we study from a few-body perspective the dynamical effects resulting from an abrupt quench or time-dependent modulation of a Hamiltonian parameter, focussing on the few-body collective excitations and the control of the dynamics. In particular, we start from strong repulsive interactions and perform negative quenches either on the interparticle repulsion or on the optical lattice depth. This permits us to unravel the transport properties and the emergent excitation modes i.e. the local breathing and the cradle processes. Especially, for the case of a negative interaction quench we demonstrate that the cradle mode can be excited only for incommensurate setups with filling factor  $\nu > 1$ , exploiting the initial delocalization. On the other hand, for filling  $\nu < 1$  in order to access this mode we use as a tool a barrier quench, thereby enforcing the over-barrier transport which in turn can generate the cradle mode. The persistence of the dynamical modes for finite-ramp rates and long evolution times accessible in recent experiments is also shown. The concept of fidelity is extensively applied in order to study the response of the quenched system and the transition from the diabatic to the adiabatic limit. The resulting non-perturbative dynamics (large quench) is explored using the recently developed numerically exact multi-layer multi-configuration time-dependent Hartree method for bosons [24, 25] (ML-MCTDHB) which reduces in our case of a single species to MCTDHB [26, 27].

This article is organized as follows. In Sec.II we explain the setup, the basic observables and the representation of the wavefunction. Sec.III is devoted to a detailed study of the non-equilibrium quantum dynamics for two different quench protocols for incommensurable setups. We summarize and give an outlook in Sec.IV. Our computational method ML-MCTDHB is described in the Appendix.

## II. Theoretical Framework

We consider  $N$  identical bosons of mass  $m$  trapped within an  $n$ -site optical lattice along the  $x$ -direction modeled by the potential  $V_{\text{tr}}(x) = V_0 \sin^2(\frac{\pi x}{l})$  where  $l$  is the distance between successive potential minima, supplied with hard-wall boundaries at  $x = \pm nl/2$ . Transversally, the bosonic system is trapped by a uniform harmonic trapping potential with energy spacing  $\hbar\omega_{\perp}$  and oscillator length  $a_{\perp} = \sqrt{\hbar/m\omega_{\perp}}$ , yielding an effective 1D coupling strength [28]  $g_{1D} = \frac{2\hbar^2 a_0}{ma_{\perp}^2} \left(1 - \frac{|\zeta(1/2)|a_0}{\sqrt{2}a_{\perp}}\right)^{-1}$  for  $s$ -wave scattering,  $a_0$  being the 3D  $s$ -wave scattering length. The many-body Hamiltonian then reads

$$H = \sum_{i=1}^N -\frac{\hbar^2}{2m} \frac{\partial^2}{\partial x_i^2} + V_{\text{tr}}(x_i) + \sum_{i < j} V_{\text{int}}(x_i - x_j) \quad (1)$$

with the short-range contact interaction potential  $V_{\text{int}}(x_i - x_j) = g_{1D} \delta(x_i - x_j)$  between bosons located at

positions  $x_i, x_j$  represented by a Dirac  $\delta$ -function. The interaction strength can thereby be tuned by varying  $a_0$  via a Feshbach resonance [28–31] or by altering the extent  $a_{\perp}$  of the transversal confinement [28, 32, 33]. In the following, for reasons of universality as well as of computational convenience we shall use dimensionless units. To this end, the Hamiltonian (1) is rescaled in units of the recoil energy  $E_r = \frac{\hbar^2 k^2}{2m}$ . For our simulations we have used a sufficiently large lattice depth  $V_0 = 6.0$  which is of the order of 3.0 to 4.0  $E_r$  (depending on  $k$ ), such that each well contains at least two localized single-particle Wannier states. The spatial and temporal coordinates are given in units of  $k^{-1}$  and  $\hbar E_r^{-1}$ , respectively.

A quench is performed by varying, abruptly or slowly, a parameter  $\lambda$  of the system (here, the interaction strength  $g_{1D}$  or the lattice depth  $V_0$ , or generally both) from an initial value  $\lambda_0 = \lambda(t=0)$  to a final value  $\lambda_f$  according to a given scheme  $\lambda(t)$ . The ground state  $|\Psi_0\rangle$  of the initial Hamiltonian  $H_0 = H(\lambda_0)$  then evolves into  $|\Psi_{\lambda}(t)\rangle = U_{\lambda}(t) |\Psi_0\rangle = \exp(-iH_{\lambda}t/\hbar) |\Psi_0\rangle$  at time  $t$  under the  $\lambda$ -quenched Hamiltonian. The overlap between the time-evolved states of the system in the presence (via  $U_{\lambda}$ ) and absence (via  $U_0 = e^{-iH_0t/\hbar}$ ) of the quench,

$$f_{\lambda}(t) = \langle \Psi_0(t) | \Psi_{\lambda}(t) \rangle, \quad (2)$$

yields the fidelity (or Loschmidt echo [34])

$$F_{\lambda}(t) = |f_{\lambda}(t)|^2, \quad (3)$$

which provides a time-resolved measure for the effect of the quench on the system.

Using the ML-MCTDHB method outlined in the Appendix, we obtain the reduced one-body density matrix

$$\rho^{(1)}(x, x'; t) = \sum_{a=0}^{M-1} n_a(t) \varphi_a(x, t) \varphi_a^*(x', t) \quad (4)$$

in its (diagonal) spectral representation by natural orbitals  $\varphi_{\alpha}(x, t)$ , where  $\alpha = 0, 1, \dots, M-1$  and  $M$  being the number of the considered orbitals. The corresponding population eigenvalues  $n_{\alpha}(t) \in [0, 1]$  characterize the fragmentation of the system [35–38]: If there is only one macroscopically occupied orbital the system is said to be condensed, otherwise it is fragmented.

To explore the spatially resolved system dynamics we use the deviation

$$\delta\rho(x, t) = \rho(x, t) - \langle \rho(x) \rangle_T \quad (5)$$

of the one-body density  $\rho(x, t) \equiv \rho^{(1)}(x, x; t)$  from its time-average  $\langle \rho(x) \rangle_T = \int_0^T dt \rho(x, t)/T$  over the considered time of propagation  $T$ . In this sense, we treat  $\delta\rho(x, t)$  as the temporal fluctuation of the density around its “macroscopic” component along the lattice.

To incorporate the information of excited bands, we further analyze the dynamics by projecting the many-body wavefunction  $\Psi$  to the multiband Wannier number

TABLE I. Energetic decomposition of some frequently used number states for  $n = 3$  lattice sites. The index  $I$  refers to the excitation order and is used as a compact notation instead of the detailed decomposition. Each element  $N^i$  in a decomposition refers to the  $i$ -th energy level (superscript) of  $N$  non-interacting bosons in the corresponding site.

index $I$	$ 2, 1, 1\rangle_I$	$ 1, 2, 1\rangle_I$
$I = 0$	$ 2^0, 1^0, 1^0\rangle$	$ 1^0, 2^0, 1^0\rangle$
$I = 1$	$ 1^0 \otimes 1^1, 1^0, 1^0\rangle$	$ 1^1, 2^0, 1^0\rangle$
$I = 2$	$ 2^0, 1^1, 1^0\rangle$	$ 1^0, 1^0 \otimes 1^1, 1^0\rangle$
$I = 3$	$ 2^0, 1^0, 1^2\rangle$	$ 1^0, 2^0, 1^1\rangle$
$I = 4$	$ 1^1 \otimes 1^2, 1^0, 1^0\rangle$	$ 1^2, 2^0, 1^0\rangle$
$I = 5$	$ 2^0, 1^2, 1^0\rangle$	$ 1^0, 1^0 \otimes 1^2, 1^0\rangle$

state basis as

$$|\Psi\rangle = \sum_{N,I} C_{N,I} |N_1 N_2 \cdots N_n\rangle_I, \quad (6)$$

where  $\{|N_1 N_2 \cdots N_n\rangle_I\}$  is the multiband Wannier number state with  $N = \sum_i N_i$ , and  $I$  indexing the energetic (excitation) order [14]. This representation proves convenient for lattice systems when describing intraband and interband processes where the spatial localization of states plays a significant role and remains valid in the strong interaction regime for a sufficient number of supplied single-particle functions. Table I presents the excitation decomposition (the occupation of excited levels in each lattice site) of some number states frequently used in the following analysis.

Note that, the eigenstates can be ordered with respect to the single particle excitation and the spatial occupation of the particles. The eigenstates of the same category form an energetical band. Following this categorization we label the eigenstates as  $|\zeta\rangle_{\alpha,I}$ , where  $\alpha, I$  denote the spatial occupation and energetical order respectively [14]. For instance  $\alpha = 1$  refers to a single-pair state,  $\alpha = 2$  to a two-pair state etc, while  $\zeta$  sorts the eigenstates within each category according to the eigenenergy.

### III. Quench dynamics

Before exploring the dynamics, some remarks concerning the ground states in the lattice for different filling factors  $\nu = N/n$ , where  $N$  denotes the particle number and  $n$  the number of the wells, are in order. For the commensurate case ( $\nu = 1, 2, \dots$ ), concerning the ground

state it is known that for increasing interparticle interaction one can realize the superfluid to Mott insulator phase transition [39] which has been addressed extensively in the past years. On the other hand, for a system with an incommensurate filling  $\nu \neq 1, 2, \dots$  the main feature is the existence of a delocalized fraction of particles which forbids the occurrence of a Mott state. Here, one can distinguish two physical situations: (a) the case  $\nu > 1$  where on-site interaction effects prevail and (b)  $\nu < 1$  in which the main concern is the redistribution of the particles over the sites as the interaction increases. This delocalized phase can also be explained in terms of the particle hole states using a strong coupling expansion [40, 41].

In the present study we consider the quench dynamics for setups with site occupancy different from unity and therefore exclude the Mott state physics. We proceed with a short reference to the ground state and consequently analyze the dynamical process following each quench protocol.

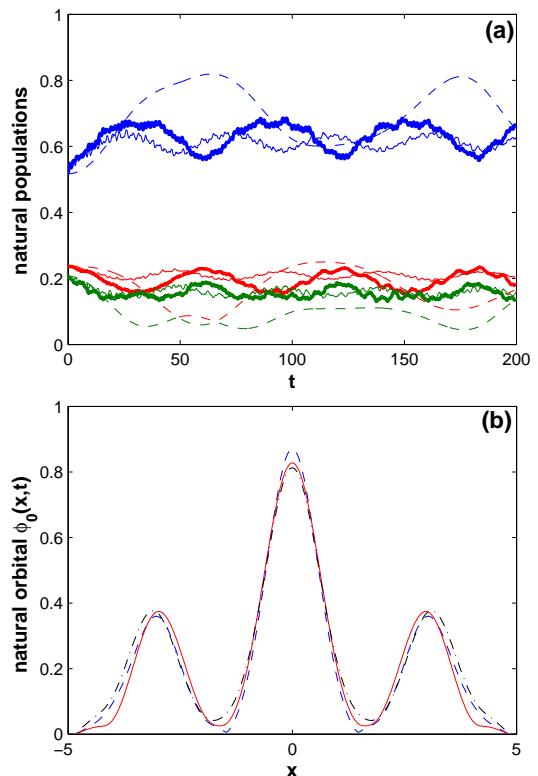


FIG. 1. (Color online) Fragmentation analysis for a system of four bosons in a triple-well with  $g_{in} = 5.0$ . Shown are (a) the time evolution of the first three occupations  $n_0(t)$  (upper panel blue lines),  $n_1(t)$  (lower panel red lines) and  $n_2(t)$  (lower panel green lines), for different quench amplitudes  $\delta g = -4.9$  (dashed lines),  $\delta g = -4.0$  (thick solid lines) and  $\delta g = -2.5$  (thin solid lines). (b) Profiles of the lowest natural orbital  $\phi_0(x, t)$  for a quench amplitude  $\delta g = -4.95$  and different time instants during the evolution  $t_1 = 0.9$  (blue dashed),  $t_2 = 2.6$  (red solid) and  $t_3 = 7.0$  (black dashed-dotted).

### A. Quench from strong to weak interactions for filling $\nu > 1$

In this section, we focus on a system consisting of four strongly interacting bosons in a triple-well, i.e. with filling  $\nu > 1$ . The initial state before the quench is characterized by the competition between delocalization and on-site interaction effects. For strong interparticle repulsion, as we consider here ( $g = 5.0$ ), this state can be interpreted as a fraction  $N \bmod n$  of extra delocalized particles being on a commensurate background of localized particles. On the one-body level the on-site populations are quite similar which can be attributed to the localized background, while their slight discrepancy is due to the non-uniform distribution of the extra particle in the first excited band. The latter prevents the formation of a perfect insulator phase even for strong repulsion. Our goal is to investigate the dynamical processes following a negative quench of the interaction strength, thereby approaching the weakly interacting regime. For an interaction quench protocol the final Hamiltonian  $H_f$  can be constructed as a sum of a part  $H_0$  which provides the pre-quenched state of the system and an additional part that denotes the perturbation

$$H_f(g_f, V) = H_0(g_{in}, V) + \frac{\delta g}{g_{in}} \sum_{k < j} V_{int}(x_k - x_j), \quad (7)$$

where  $g_{in}$  and  $g_f$  are the initial and final interaction strengths respectively, and  $\delta g = g_f - g_{in}$  is the quench amplitude focussing here on  $\delta g < 0$  and  $\left| \frac{\delta g}{g_{in}} \right| \sim 1$ .

In the following subsections we first proceed with a brief fragmentation analysis inspired from the perspective of natural orbitals. Then, we explain in some detail the response of the system and investigate each of the emergent normal modes consisting of a local breathing mode and a dipole-like cradle mode. A study for the manipulation of the excited modes and their presence for the case of a finite ramp is also provided.

#### 1. Dynamical fragmentation

In this subsection, we analyze the role of dynamical fragmentation, i.e. the occurrence of more than one significantly occupied quantum states during the evolution, with a varying quench amplitude. Especially, the fragmentation in the non-equilibrium dynamics of trapped finite systems is known to depend strongly on the particle number [37, 42], the interaction strength and the evolution time. The spectral decomposition of the one-body reduced density matrix offers a measure of fragmentation via the populations  $n_a(t)$  of the natural orbitals  $\phi_a(t)$  (see eq.(4)). In particular, a non-fragmented (condensed) state requires the occupation of  $n_0(t)$  to be close to unity [38].

Figure 1(a) shows the evolution of the natural populations of the three highest occupied natural orbitals for

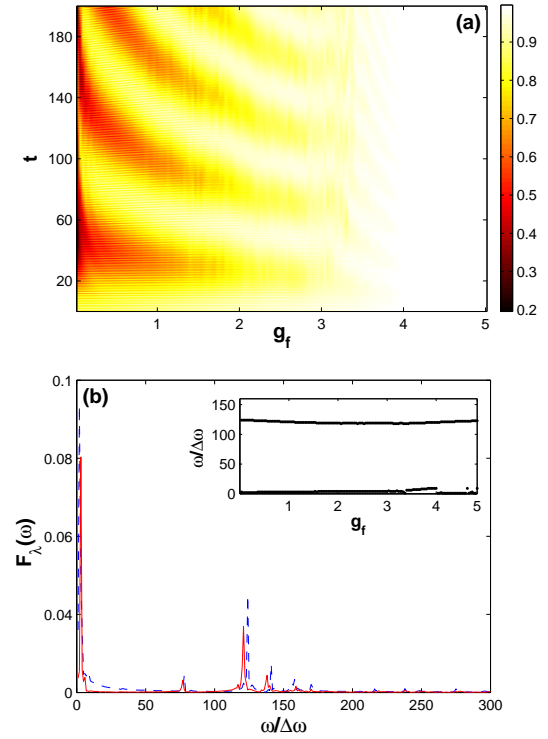


FIG. 2. (Color online) (a) Fidelity evolution following negative interaction quenches for  $g_{in} = 5.0$ . (b) The frequency spectrum of the fidelity for  $g_f = 0.6$  (blue dashed) and  $g_f = 1.0$  (red solid), which indicates the tunneling modes. The inset shows the dependence of each tunneling branch with respect to the final interaction strength after the quench. We incorporate 150 quenches in the range of  $0 < g_f < 5.0$ . The frequency units are normalized as  $\omega/\Delta\omega$ , with  $\Delta\omega = 2\pi/T$  and  $T$  being the considered evolution time.

different quench amplitudes. The population of the first orbital  $n_0(t)$  is always significantly below unity which confirms the fragmentation process, while the three most occupied natural orbitals add up to more than 90% of the population. Focussing on the first orbital we note that the temporal average of the fragmentation reduces as the quench amplitude increases and vice versa. Especially, for final interactions close to a non-interacting state we observe a tendency for a non-fragmented state at least for certain time periods. This constitutes a major difference between a negative and a positive interaction quench scenario. In the latter case the fragmentation process is enhanced for larger quench amplitudes which can be attributed to the consequent raise of the interparticle repulsion during the process. However, here we face the inverse behaviour because in the initial strongly interacting state the interparticle repulsion is already significant and tends to be reduced after the quench. Moreover, the second and third orbitals take on a compensatory role to the first, e.g. in the time periods where  $n_0(t)$  is enhanced  $n_1(t)$  and  $n_2(t)$  are reduced. Finally, note that for smaller quenches the latter populations possess smaller

amplitude oscillations whereas strong quenches introduce large amplitude variations of the populations.

Figure 1(b) illustrates the response of the first natural orbital  $\phi_0(x, t)$  at different time-instants during the evolution after a quench to  $g_f = 0.05$ . As it can be seen  $\phi_0(x, t)$  exhibits spatial oscillations in the outer wells and an on-site broadening in the middle well which accounts for interaction effects. Another important remark is that the band-structure is effectively reflected by the population of the natural orbitals, i.e. the orbitals  $\phi_0(x)$ ,  $\phi_1(x)$  and  $\phi_2(x)$  correspond to the effective first single-particle band, orbitals  $\phi_3(x)$ ,  $\phi_4(x)$  and  $\phi_5(x)$  to the second band etc. Thus, the lowest orbital  $\phi_0(x, t)$  follows quite well the evolution of the quenched one-body density.

## 2. Dynamical response and transport properties

To investigate the dynamical response of the system we use the above-discussed fidelity  $F_\lambda(t)$  (see eq.(3)). This quantity is shown in Figure 2(a) as a function of the final interaction strength and the time. We mainly note the appearance of two different regions as a function of the quench amplitude. The first one corresponds to quenches from a strong repulsive state with  $g_{in} = 5.0$  to intermediate interactions where  $3.4 < g_f < 5.0$ . Here, the overlap during the dynamics is rather large with minimal percentage up to 85% and therefore the system is quite insensitive to the quench. In the second region where the final state belongs to weak or even to the non-interacting regime, i.e.  $0 < g_f < 3.4$ , we observe the formation of an oscillatory pattern in the fidelity evolution. This pattern indicates the sensitivity of the system to these type of quenches meaning that the system can be driven far from the initial state, while the minimal overlap for the extreme case of  $g_f \rightarrow 0$  can even be of the order of 20%. The emergence of the above regions is universal in the system in the sense that it weakly depends on the height of the barrier. Thus, for an increasing barrier height the second region (larger quenches) will become narrower due to the larger potential energy which inhibits a possible departure of the system from the initial state.

In order to identify the tunneling modes participating in the dynamics we use as a measure the spectrum of the fidelity  $F_\lambda(\omega) = \frac{1}{\pi} \int dt F_\lambda(t) e^{i\omega t}$ . Indeed, Figure 2(b) shows  $F_\lambda(\omega)$  for different final interactions where we observe two dominant tunneling peaks. To proceed with a more quantitative description of the tunneling dynamics we shall expand the wavefunction in terms of the number states. To this end, let  $|\Psi(0)\rangle = \sum_{\zeta; \alpha; I} C_\zeta^{\alpha; I} |\zeta\rangle_{\alpha; I}$  be the initial wavefunction in terms of the eigenstates  $|\zeta\rangle_{\alpha; I}$  of the final Hamiltonian [14]. Then, the expansion of the

fidelity reads

$$|\langle \Psi(0) | \Psi(t) \rangle|^2 = \sum_{\zeta_1; \alpha; I} |C_{\zeta_1}^{\alpha; I}|^4 + \sum_{\zeta_1, \zeta_2; \alpha, \beta; I} |C_{\zeta_1}^{\alpha; I}|^2 |C_{\zeta_2}^{\beta; I}|^2 \cos(\epsilon_{\zeta_1}^{\alpha; I} - \epsilon_{\zeta_2}^{\beta; I})t, \quad (8)$$

where the second term contains the separate contributions from each tunneling branch. The indices  $\alpha, \beta$  indicate a particular set of number states,  $\zeta_i$  is the intrinsic index within each set,  $I$  denotes the respective energetical level and  $\epsilon_{\zeta_i}^{\alpha; I}$  refers to the eigenfrequency of a particular eigenstate. In particular, the first peak at frequency  $\omega_1 \approx 3\Delta\omega$  (with  $\Delta\omega = 2\pi/T$  and  $T$  denotes the propagation time) corresponds to the energy difference  $\Delta\epsilon$  within the energetically lowest states of the single pair mode. Therefore the process corresponds to an intraband tunneling, e.g. from the state  $|1, 2, 1\rangle_0$  to  $|2, 1, 1\rangle_0$  etc. However, the second peak located at  $\omega_2 \approx 125\Delta\omega$  refers to an interband transition between the states  $|1, 2, 1\rangle_2$  and  $|1, 2, 1\rangle_0$ , which reflects the initial strongly correlated state. In the inset we present the  $\delta g$ -dependence of the location of the aforementioned peaks. As it can be seen the two branches are mainly steady as a function of the interaction quench, their frequencies are constrained in a narrow-band, while their amplitude (see main Figure) reduces significantly for weak quenches.

In the course of the investigation of the tunneling dynamics one fundamental question that has to be addressed is how correlations propagate [43] in the quenched system. Here, in order to distinguish genuine interwell correlations from density oscillation effects we explore the response of the normalized single particle correlations  $g_{ij}^{(1)}(t) = \langle \Psi | b_i b_j^\dagger | \Psi \rangle / \sqrt{\langle \Psi | b_i b_i^\dagger | \Psi \rangle \langle \Psi | b_j b_j^\dagger | \Psi \rangle}$  [44].  $b_i^\dagger$  denotes the creation operator of a particle at the  $i$ -th well, while the diagonal elements  $g_{ii}^{(1)} = 1$  by definition. An important property of this function is that for  $g_{ij}^{(1)} > 1$  ( $< 1$ ) the corresponding detection probabilities at positions  $i$  and  $j$  are correlated (anticorrelated), while the case  $g_{ij}^{(1)} = 1$  is referred to as fully first order coherent. Figures 3(a)-(c) illustrate the time evolution for different components of the one-body correlations for various negative interaction quenches. As expected the diagonal terms correspond to a straight line at unity for all quench amplitudes. The non-diagonal terms  $g_{ij}^{(1)}, i \neq j$  exhibit a non-vanishing oscillatory behaviour, while for increasing quench amplitude a substantial built-up of correlations is observed. In particular, approaching the non-interacting limit  $g_{LM}^{(1)}(t) > 1$  for most of the time, whereas  $g_{LR}^{(1)}(t)$  oscillates around unity indicating a transition from an anticorrelated to a correlated situation.

## 3. The local breathing mode

The breathing mode can be used in order to measure some key quantities of a trapped system such as its ki-

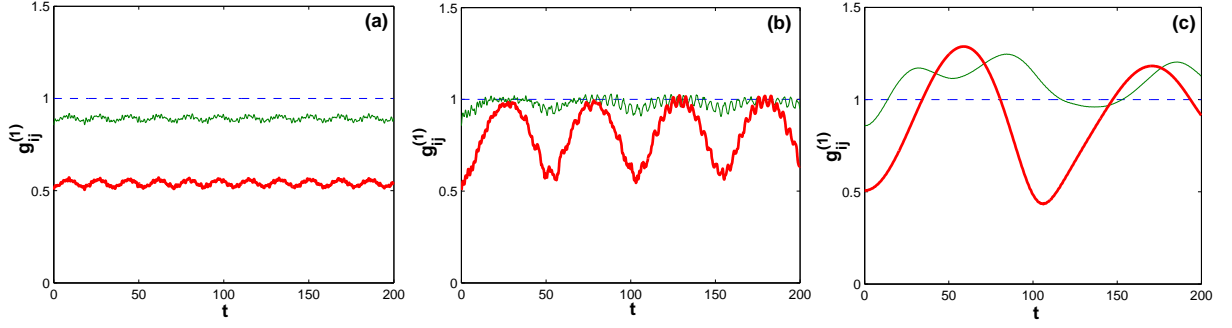


FIG. 3. (Color online) The time evolution of the one-body correlation function  $g_{ij}^{(1)}$  after various negative interaction quenches for  $g_{in} = 5.0$ . Shown are different components of the correlation function  $g_{ij}^{(1)}$  with respect to the left well  $g_{LL}^{(1)}$  (blue dashed line),  $g_{LM}^{(1)}$  (green thin solid line) and  $g_{LR}^{(1)}$  (red thick solid line) for final interactions (a)  $g_f = 3.8$ , (b)  $g_f = 1.6$  and (c)  $g_f = 0.05$ .

netic and interaction energy or the coupling strength [17–19]. It refers to an expansion and contraction of the bosonic cloud and can be excited either via a variation of the interparticle interaction or a modulation of the frequency of the trapping potential.

In a similar manner, our quenched system exhibits local breathing oscillations which are most prominent in the subsystem corresponding to the middle well. To detect the frequencies of this normal mode we examine the variance of the coordinate of the center of mass for a particular well. The center of mass for the  $i$ -th well is defined as  $X_{CM}^{(i)} = \int_{d_i}^{d'_i} dx (x - x_0^{(i)}) \rho_i(x) / \int_{d_i}^{d'_i} dx \rho_i(x)$ . The index  $i = R, M, L$  corresponds to the right, middle and left well respectively, while  $x_0^{(i)}$  refers to the central point of the corresponding well. The limits of the wells are denoted by  $d_i$  and  $d'_i$ , whereas  $\rho_i(x)$  is the respective single particle density. For the identification of the breathing process we define the operator of the second moment  $\sigma_M^2(t) = \langle \Psi | (x - X_{CM}^{(i)})^2 | \Psi \rangle$ . The latter serves as a measure for the instantaneous spreading of the cloud in the  $i$ -th well and can also be used experimentally in order to probe the expansion velocity of a quenched condensate [5]. Then, if we connect the initial wavefunction with the eigenstates  $|\zeta\rangle_{\alpha;I}$  of the final Hamiltonian  $H_f$ , we obtain

$$\begin{aligned} \sigma_M^2(t) = & \sum_{\alpha; \zeta_1; I} \left| C_{\zeta_1}^{\alpha; I} \right|^2_{\alpha; I} \langle \zeta_1 | (x - X_{CM}^{(i)})^2 | \zeta_1 \rangle_{\alpha; I} \\ & + 2 \sum_{\zeta_1 \neq \zeta_2} \text{Re} \left( C_{\zeta_1}^{\beta; I*} C_{\zeta_2}^{\alpha; I} \right)_{\beta; I} \langle \zeta_1 | (x - X_{CM}^{(i)})^2 | \zeta_2 \rangle_{\alpha; I} \\ & \times \cos \left( \omega_{\zeta_1}^{\beta; I} - \omega_{\zeta_2}^{\alpha; I} \right) t. \end{aligned} \quad (9)$$

To identify the frequencies of the local breathing mode Figure 4 shows the frequency spectrum of the second moment  $\sigma_M^2(\omega) = \frac{1}{\pi} \int dt \sigma_M^2(t) e^{i\omega t}$ , which refers to the middle well, for different quench amplitudes. Three main

peaks can be observed. The lowest of these three peaks refers to a tunneling mode being identified from the energy difference within the energetically lowest states of the single pair mode. The appearance of this peak in the spectrum is due to the fact that the tunneling can induce a change in the width of the local wavepacket. The second and third peaks refer to interband processes and are related to higher-band transitions. In particular, the second peak is located at  $\omega_2 \approx 125\Delta\omega$  and refers to a transition from  $|1, 2, 1\rangle_0$  to  $|1, 2, 1\rangle_2$ , whereas the third one with frequency  $\omega_3 \approx 170\Delta\omega$  corresponds to a transition from  $|1, 2, 1\rangle_0$  to  $|1, 2, 1\rangle_5$ . To illustrate the dependence of the above three peaks on the interaction quench we show in the inset the evolution of the location of each peak with respect to the final interaction strength  $g_f$  after the quench. We observe that the branches are more sensitive for a quench to  $2.0 < g_f < 4.0$ , otherwise they are mainly constant.

#### 4. The cradle mode

This mode refers to a dipole-like oscillation generated via an over-barrier transport due to the initially delocalized state between neighboring wells. In the present case it is induced by an interaction quench. From a one-body perspective the cradle mode is demonstrated by the inner well dynamics of the one-body density fluctuations  $\delta\rho(x, t)$ . Figure 5 shows the evolution of the system through the relative density after a sudden negative interaction quench from  $g_{in} = 5.0$  to  $g_f = 0.07$ . The emergence of the cradle mode in the outer wells manifested as a dipole-like oscillation and the local breathing in the central well as a contraction and expansion dynamics is observed.

The initial spatial configuration due to the strong interparticle interaction corresponds to one localized boson in each well and one delocalized (over the three wells) energetically close to the barrier. In turn, the negative change in the interaction strength yields a high proba-



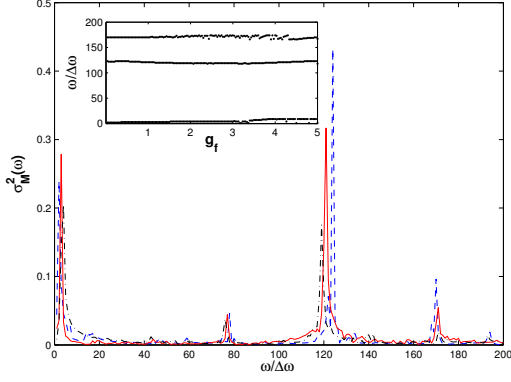


FIG. 4. (Color online) Fourier spectrum of the second moment  $\sigma_M^2(\omega)$  for the local breathing mode for different quench amplitudes. The initial state corresponds to  $g_{in} = 5.0$  and the final interactions are  $g_f = 0.15$  (blue dashed),  $g_f = 0.8$  (red solid), and  $g_f = 1.7$  (black dashed-dotted). In the inset we show the  $\delta g$ -dependence of each breathing branch, where we incorporate 150 quenches in the range of  $0 < g_f < 5.0$ . Note that the frequency units are normalized with respect to  $\omega/\Delta\omega$ , where  $\Delta\omega = 2\pi/T$  and  $T$  is the respective propagation time.

bility for the delocalized particle to overcome the barrier (over-barrier transport) and move to a neighboring well, where it performs a collision with the initially localized particle. This results in the cradle-like mode inside the respective neighboring site and refers to a localized wavepacket oscillation [14]. Note that the cradle is inherently related to the initial delocalization and after a negative interaction quench of a strongly correlated system can be excited only for incommensurate systems with filling factor  $\nu > 1$ . For other fillings it disappears and the consequent dynamics is dominated by the interwell tunneling.

In the following, in order to quantitatively examine the inner-well dynamics we proceed with a local density analysis. For that purpose we divide a particular well from the center into two equal sections with  $\rho_{a,1}(t)$  and  $\rho_{a,2}(t)$  being the respective integrated densities of the left and right parts during the evolution. The index  $a = L, M, R$  stands for the left, middle and right well respectively. In this manner, a measure of the intrawell asymmetry which captures the cradle motion is the quantity  $\Delta\rho_a(t) = \rho_{a,1}(t) - \rho_{a,2}(t)$ . Figure 6(a) shows the frequency spectrum of the above quantity for the left well, i.e.  $\Delta\rho_L(\omega) = \frac{1}{\pi} \int dt \Delta\rho_L(t) e^{i\omega t}$  for various negative interaction quenches. From the spectrum we can identify two dominant peaks located at the positions  $\omega_2 \approx 79\Delta\omega$  and  $\omega_3 \approx 125\Delta\omega$ . These two frequency branches correspond to the cradle mode. In addition, we observe a low-frequency peak related to the interwell tunneling at frequency  $\omega_1 \approx 3\Delta\omega$ . The inset shows the  $\delta g$ -dependence of the above three frequency peaks. The location of each branch remains essentially independent of the strength of the interaction quench and it is therefore constrained

to a corresponding narrow-band.

To gain a deeper understanding of the cradle mode we again refer to a number state analysis and expand the initial state of the system in terms of the eigenstates of the final Hamiltonian as  $|\Psi(0)\rangle = \sum_{\zeta;\alpha;I} C_{\zeta}^{\alpha;I} |\zeta\rangle_{\alpha;I}$ . Then, the expectation value of the asymmetry operator reads

$$\begin{aligned} \langle \Psi | \Delta\hat{\rho}(t) | \Psi \rangle &= \sum_{\zeta_1;\alpha;I} \left| C_{\zeta_1}^{\alpha;I} \right|^2 I_{;\alpha} \langle \zeta_1 | \Delta\hat{\rho} | \zeta_1 \rangle_{\alpha;I} \\ &+ 2 \sum_{\zeta_1 \neq \zeta_2} \text{Re} \left( C_{\zeta_1}^{\alpha;I*} C_{\zeta_2}^{\beta;I} \right) I_{;\alpha} \langle \zeta_1 | \Delta\hat{\rho} | \zeta_2 \rangle_{\beta;I} \quad (10) \\ &\times \cos \left[ \left( \omega_{\zeta_1}^{\alpha;I} - \omega_{\zeta_2}^{\beta;I} \right) t \right]. \end{aligned}$$

Here the terms of the second sum in the above expression which demonstrate an oscillatory behaviour describe the cradle mode. Therefore, we need to detect the eigenstates ( $|\zeta\rangle_{\alpha;I}$ ) of the dominant oscillation terms, i.e.  $\alpha;I \langle \zeta | \Delta\hat{\rho} | \zeta \rangle_{\beta;I} \neq 0$ . A direct numerical analysis indicates that the respective eigenstates are  $|\zeta\rangle_{1;0}$ ,  $|\zeta\rangle_{1;1}$ ,  $|\zeta\rangle_{1;2}$ , whereas the corresponding significantly contributing number states are  $|2, 1, 1\rangle_0$ ,  $|2, 1, 1\rangle_1$  and  $|2, 1, 1\rangle_4$  due to the fact that the corresponding oscillation frequency matches the energy difference between these eigenstates.

Let us now, investigate possible control protocols of the cradle mode via a modulation of its frequency by means of a varying potential parameter or via an external forcing. An efficient way to manipulate the frequency is to tune the height of the potential barriers. In this way, the cradle frequency can be reduced using a more shallow lattice (thereby making the excitation of the cradle mode more easy). Indeed, within the harmonic approximation it can be easily shown that the effective frequencies for two lattices with different potential depths  $V_{0;1}$  and  $V_{0;2}$ , respectively, obey  $\omega_{eff;1} = (V_{0;1}/V_{0;2})^{1/4} \omega_{eff;2}$ . This situation is illustrated in Figure 6(b) where the frequency spectrum of the inner-well asymmetry with the same quench amplitude but different barrier heights  $V_0 = 5.5$  (red solid) and  $V_0 = 3.5$  (blue dashed) is shown. We observe a negative shift of each frequency peak for a decreasing lattice depth which confirms our previous arguments. Alternatively, a similar manipulation of the cradle frequency can be achieved by comparing lattices with the same height of the potential barrier but different frequencies. Then, the respective effective frequencies are related via  $\omega_{eff;1} = (l_2/l_1)^{1/2} \omega_{eff;2}$ , where  $l$  is the distance between two successive potential minima.

In a similar manner, one can pose the question how the cradle mode frequency depends on  $g_{in}$  for fixed  $g_f$ . According to our simulations (omitted here for brevity) each peak remains essentially unchanged, indicating that the system does not keep any memory from the particular strongly correlated initial microscopic configuration.

A further question is to ask for the impact of the boundary conditions. Hence, we assume a fixed height

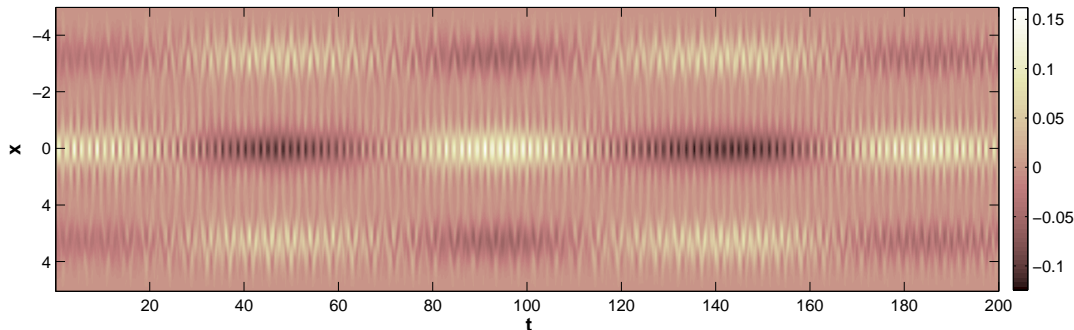


FIG. 5. (Color online) Space-time evolution of the fluctuations  $\delta\rho(x, t)$  after a sudden negative quench of the inter-particle repulsion from  $g_{in} = 5.0$  to  $g_f = 0.07$ , thereby approaching the non-interacting limit. We observe the cradle mode in the left and right wells, the local breathing mode in the middle well and the interwell tunneling during the evolution.

for the barrier but changing the position of the hard wall boundary conditions. Then, we expect that as the wall is closer to the center of the right or left well the cradle would be more enhanced because effectively the frequency of the local harmonic oscillator is larger and so the period of the cradle reduces. Indeed, Figure 6(c) illustrates for the same quench amplitude the Fourier spectrum of the intrawell asymmetry  $\Delta\rho_L(\omega)$  imposing the hard-wall boundaries at different positions, namely at  $x_\sigma = \pm 3\pi/2$  (blue dashed),  $x_\sigma = \pm 5\pi/4$  (red solid) and  $x_\sigma = \pm 11\pi/8$  (black dashed-dotted). The frequency peaks of the cradle mode are shifted by a positive value for a closer to the center hard-wall. As a final attempt we impose a harmonic trap on top of the triple well, which increases the potential energy of the edge wells. Then the on-site energy of the Wannier states at the edges becomes larger than that (of the same degree of energetical excitation) in the central well. This in turn renders the initialization of the cradle mode more difficult, and for strong superimposed harmonic traps its excitation for a fixed quench amplitude becomes impossible. Accordingly, Figure 6(d) shows a scenario with the same quench amplitude but different superimposed harmonic traps. We observe negative variations and a reduction of the intensity of each peak for a stronger harmonic trap, thereby confirming our above discussion.

In the next subsection we explore the excitation modes induced by a time-dependent modulation of the interaction strength and establish their presence also for this case.

### 5. Finite ramping

The present subsection is devoted to the study of the dynamics induced by time-dependent interaction quenches with a finite ramp-rate. In particular, we attempt to investigate quenches with the same amplitude but evolving on different time-scales, in order to gain a further insight into the dynamical response of the system with relevance to the experimentally occurring time-

scales. To this end, let us adopt a time-dependent quench scenario of the form

$$g(t; \tau) = g_{in} + (g_f - g_{in}) \tanh(t/\tau). \quad (11)$$

Here  $g_{in}$ ,  $g_f$  are the interaction strength for the initial and final state respectively, whereas  $\tau$  denotes the finite ramp-rate of the performed quench. Focussing now on a strong non-equilibrium post-quench state with  $g_f = 0.1$ , Figure 7 shows the dynamical crossover, for finite evolution times, from an abrupt to an adiabatic interaction modulation for increasing ramp-rates  $\tau$ . To interpret the resulting behaviour on a relevant time-scale we define the Heisenberg time  $\tau_H \sim 1/\Delta\epsilon(\delta g)$ , where  $\Delta\epsilon(\delta g) = \epsilon(g_{in}) - \epsilon(g_f)$  refers to the energy difference between the ground state of the system before and after a sudden interaction quench. As it is shown for times  $t < \tau$  (region under the black dotted line in Figure 7) the system essentially remains in the initial ground state of the unperturbed Hamiltonian. On the contrary, in the region with  $t > \tau$ , which spreads for decreasing  $\tau$  (thereby approaching the sudden quench), the system starts to significantly depart from the initial state. Remarkably enough for  $\tau < 30\tau_H$  we observe the appearance of black lobes (overlap of the order of 40%) during the evolution which indicate the persistence of the excitation modes in this region. For  $\tau > 30\tau_H$  we have a transition to a smoother dynamical departure of the system from the initial state and as a consequence the elimination of the excitation modes. In particular, for  $\tau > 85\tau_H$  the Hamiltonian changes sufficiently slowly, i.e. the system tends to remain in the instantaneous ground state and therefore the modulation is almost adiabatic for the whole evolution time. For a smaller quench the adiabatic regime can be reached for sufficiently smaller time-scales due to the reduced impact of the quench to the system. These statements are also valid for a linear quench protocol of the form  $g(t; \tau) = g_{in} + (g_f - g_{in})t/\tau$  for  $t \leq \tau$ , and  $g(t; \tau) = g_f$  for  $t > \tau$ .

As a next step we study the effect of the time-dependent interaction quench on the excitation modes, i.e. the breathing and cradle processes. To give further



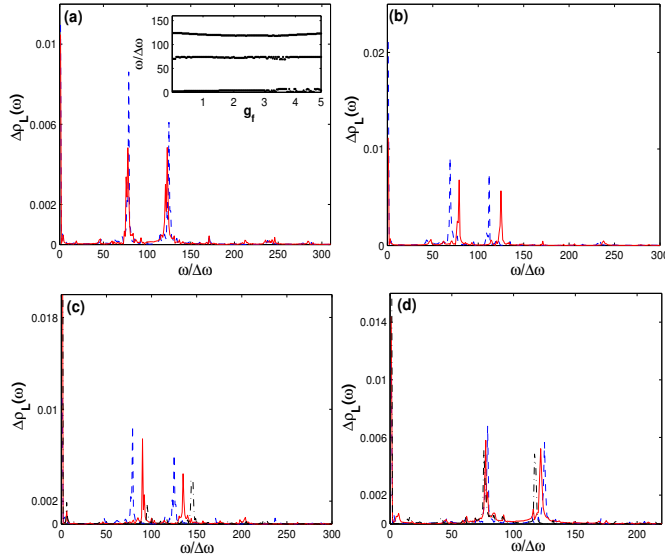


FIG. 6. (Color online) The frequency spectrum of the intrawell asymmetry  $\Delta\rho_L(\omega)$ . (a) The final state of the system is obtained after a sudden negative interaction quench from  $g_{in} = 5.0$  to  $g_f = 0.1$  (blue dashed) and  $g_f = 0.45$  (red solid). The inset shows the evolution of each peak that refers to the cradle as a function of the quench amplitude (we incorporate 150 quenches in the range  $0 < g_f < 5.0$ ). (b) The spectrum  $\Delta\rho_L(\omega)$  for the same quench amplitude,  $\delta g = -4.95$ , and different barrier heights  $V_0 = 5.5$  (red solid) and  $V_0 = 3.5$  (blue dashed). (c) Sudden quench to  $g_f = 0.4$  and the hard-wall boundaries located at  $x_\sigma = \pm 3\pi/2$  (blue dashed),  $x_\sigma = \pm 5\pi/4$  (red solid) and  $x_\sigma = \pm 11\pi/8$  (black dashed-dotted). (d) It is illustrated the spectrum of  $\Delta\rho_L(\omega)$  for an imposed harmonic trap  $V_{harm} = 0$  (blue dashed),  $V_{harm} = 0.02x^2$  (red solid) and  $V_{harm} = 0.05x^2$  (black dashed-dotted) on top of the lattice. Finally, note that in each case we use normalized frequency units  $\omega/\Delta\omega$ , with  $\Delta\omega = 2\pi/T$  and  $T$  being the respective evolution time.

insight in the overall non-equilibrium process Figure 8 illustrates the evolution of  $\delta\rho(x, t)$ , for the same relevant interactions as in Figure 5 where we considered a sudden quench, implementing now the time-dependent scenario of equation (11) with a finite rate  $\tau = 0.8\tau_H$ . The above-discussed modes still persist but with reduced intensity which is larger when the quench is faster.

According to this let us investigate how one can manipulate the local breathing mode via the quench rate  $\tau$ . Figure 9(a) shows the frequency spectrum of the local breathing mode obtained for the same amplitude  $\delta g = -4.9$  and different quench rates  $\tau$ . As it can be seen the position of each peak remains the same but its intensity decreases significantly for larger rates. To further probe the position of each branch with respect to the quench rate  $\tau$  we present in the inset the  $\tau$ -dependence of each peak (without taking into account its intensity). It is obvious that each branch is quite insensitive to the interaction quench while in terms of its intensity (Figure 9(a)), one can infer that by considering larger rates

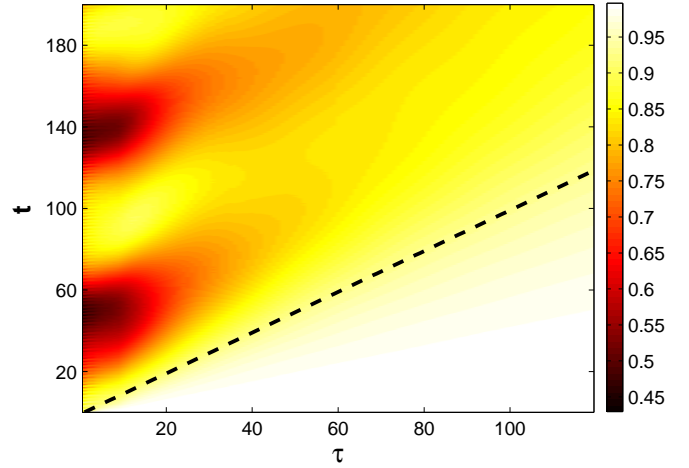


FIG. 7. (Color online) Fidelity evolution for  $g_{in} = 5.0$  and  $g_f = 0.1$  as a function of the ramp-rate  $\tau$  measured in units of the Heisenberg time  $\tau_H$  (see text). The black dotted line correspond to the situation with  $t = \tau$ .

can gradually obliterate each frequency branch, i.e. for a faster quench the spectrum is more rich. Especially, one finds that for  $\tau > 30\tau_H$  this mode can essentially be eliminated which means that the intensity of each peak is negligible (in our case  $\leq 10^{-5}$ ).

Finally, we study the effect of the finite ramping on the cradle mode. Figure 9(b) presents the spectrum of the intrawell asymmetry  $\Delta\rho_L(\omega)$  for an abrupt quench in the interparticle repulsion and two different quenches obeying the above time-dependent law with different rates  $\tau$  but same final interaction as in the abrupt case. Moreover, in the inset we demonstrate the evolution of each peak (without taking into account its intensity) as a function of the ramp-rate  $\tau$ . We observe that for larger rates  $\tau$  the location of each frequency peak remains essentially the same (inset) but the respective amplitude tends to decrease, while for  $\tau > 9.0\tau_H$  the third peak that refers to the second excited state in the left well has already been eliminated. Increasing further the rate  $\tau > 30\tau_H$  one can eliminate the cradle (intensity  $\leq 10^{-5}$ ) approaching the adiabatic region as also shown in Figure 7.

In the following section we turn to the study of the quench dynamics induced by a modulation of the optical lattice depth examining its dynamical response and the consequent excitation modes.

## B. Quench of the optical potential depth for filling $\nu < 1$

Here we consider a quench protocol which consists of a ramp-down of the optical potential depth, thereby driving the system to a region where the kinetic energy of the atoms dominates in comparison to the potential energy. As we shall demonstrate, following this protocol

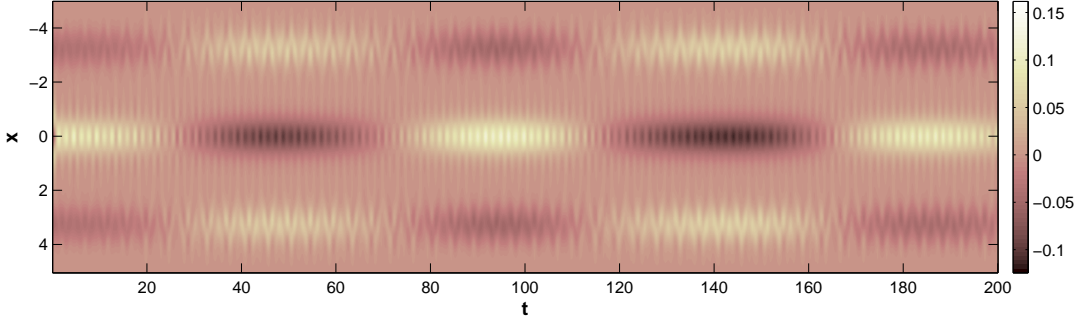


FIG. 8. (Color online) The fluctuations  $\delta\rho(x, t)$  of the one-body density caused by a negative time-dependent quench of the inter-particle repulsion to  $g_f = 0.07$  ( $g_{in} = 5.0$ ) with a finite ramp-rate  $\tau = 0.8\tau_H$ . For a direct comparison the quench parameters, here, have been chosen similar with Figure 5, which refers to the respective sudden quench scenario. We observe that the cradle mode in the left and right wells, the local breathing mode in the middle well and the interwell tunneling during the evolution persist.

one can excite the cradle mode also for setups with filling  $\nu < 1$ . The system consists of five particles in an eight well setup but our conclusions can be easily generalized for arbitrary filling factors. To be self-consistent with the previous study we start from a strongly interacting initial state with  $g_{in} = 5.0$ , while the lattice is assumed to be initially deep enough with a depth  $V_{0;in} = 8.0$  to include the first three Wannier energy levels. As usual, in order to interpret the dynamics induced by the quench we should be aware of the characteristics of the initial ground state. For a system with filling  $\nu < 1$  the one-body density remains asymmetric even for strong interactions due to the low population, while the delocalized fraction of particles permits the presence of long range one particle correlations even in the strongly repulsive regime [45].

Let us firstly analyze the non-equilibrium dynamics induced by a sudden ramp-down of the optical potential depth at time  $t=0$ . The final Hamiltonian that governs the dynamics following the above scenario is given by

$$H_f(g, V_{0;f}) = H_0(g, V_{0;in}) + \frac{\delta V_0}{V_{0;in}} \sum_{k=1}^N V_{tr}(x_k), \quad (12)$$

with  $V_{0;in}$ ,  $V_{0;f}$  being the initial and final potential depth respectively,  $\delta V_0 = V_{0;f} - V_{0;in} < 0$  due to the reduction of the barrier and  $V_{tr}$  being the lattice potential.

To examine the response of the system after the quench we initially rely on the fidelity  $F_\lambda(t)$ . We consider quenches of the barrier down to  $V_{0;f} = 2.0$ , where the lattice is quite shallow and includes only the first Wannier energy level while the others are considered as delocalized. Indeed, Figure 10(a) shows in a transparent way the instantaneous fidelity as a function of the final lattice depth. The rise of two different dynamical regions is observed. In the first region ( $5.0 < V_{0;f} < 8.0$ ) the overlap is rather large with a minimum of the order of 80%, while in the second region ( $2.0 < V_{0;f} < 5.0$ ) it can even reach 25% during the evolution. As we shall demonstrate below, the response of the system following this protocol

is drastically different from that obtained through an interaction quench for fillings  $\nu < 1$  where the dynamics is dominated by the interwell tunneling. In particular, one can excite more on-site dynamical modes and even use a barrier quench on top of an interaction quench in order to excite the cradle mode. To indicate the latter and also to trigger more efficiently the dynamical modes from here on we mainly proceed by performing a simultaneous barrier and an interaction quench to weak interactions, i.e.  $g_f = 0.02$ . Figure 10(b) presents the fidelity during the dynamics induced by different quenches of the lattice depth and a simultaneous interaction quench to  $g_f = 0.02$ . The dynamical response of the system shows four different regions during the evolution. In the first (white part) the system is close to the initial state with minimal percentage up to 80%, while the second (yellow) and the third (light-red) regions indicate that the system significantly departs from the initial state with a percentage of the order of 50% and 30% respectively. The latter regions correspond to transition states following the combined quench. Finally, in the fourth section (dark-red) the system is driven to a completely different state possessing a maximal overlap of the order of 10%. In particular, for a fixed overlap a quadratic response of the system as a function of the quench amplitude is observed.

To analyze further the response of the system, Figure 10(c) illustrates some profiles of the fidelity in the course of the dynamics for different quenches. The fidelity exhibits a quadratic decay for short times, while after a characteristic time  $\tau_c(\delta V_0)$  it oscillates around a constant value  $F_0(\delta V_0)$ , which depends on the quench amplitude such that it is larger for a smaller quench. The observed short-time quadratic behaviour can be easily explained as follows. Let  $|\Psi_0\rangle$  be the initial eigenstate of  $H_0$ , and  $|\Psi(\delta t)\rangle$  the corresponding state after a short-time interval  $\delta t$ . Then, the short-time expansion of the overlap

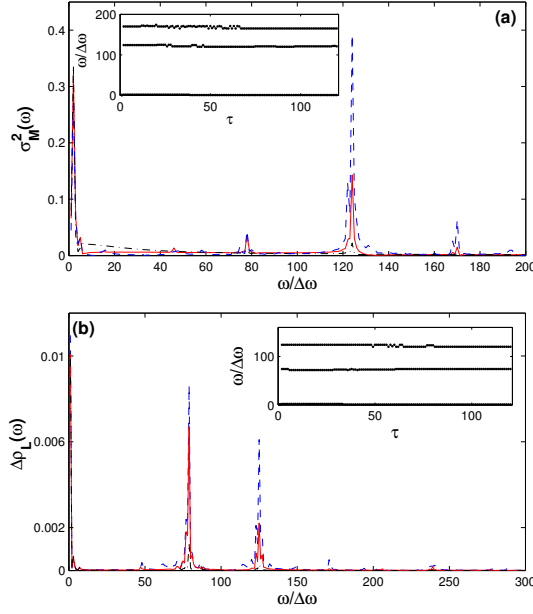


FIG. 9. (Color online) (a) Frequency spectrum of the variance  $\sigma_M^2(\omega)$  for time-dependent quenches of the form of equation (11) with final interaction  $g_f = 0.1$  and rates  $\tau = 0\tau_H$  (blue dashed),  $\tau = 0.8\tau_H$  (red solid) and  $\tau = 3.0\tau_H$  (black dashed-dotted). The inset shows each branch of the local breathing mode as a function of the quench rate  $\tau$  (we incorporate 160 different rates in the range  $0 < \tau < 120$ ). In (b) we present the spectrum of the intrawell asymmetry  $\Delta\rho_L(\omega)$  for a time-dependent scenario with quench amplitude  $\delta g = -4.90$  and rates  $\tau = 0\tau_H$  (blue dashed),  $\tau = 0.8\tau_H$  (red solid) and  $\tau = 3.0\tau_H$  (black dashed-dotted). The inset demonstrates the dependence of each branch of the cradle mode as a function of the quench rate  $\tau$ . Finally, note that we have used normalized frequency units  $\omega/\Delta\omega$ , with  $\Delta\omega = 2\pi/T$  and  $T$  being the respective evolution time.

reads

$$|\langle \Psi_0 | \Psi(\delta t) \rangle|^2 = 1 - (\delta t/\tau_c)^2 + \mathcal{O}((\delta t)^4), \quad (13)$$

$\tau_c^{-1} = (\langle \Psi(\delta t) | H_f^2 | \Psi(\delta t) \rangle - \langle \Psi(\delta t) | H_f | \Psi(\delta t) \rangle^2)^{1/2}$  is the quench characteristic time  $\tau_c(\delta V_0)$  or so-called Zeno time [34, 46]. Especially, we observe that the time  $\tau_c(\delta V_0)$  depends on the quench amplitude, i.e. for smaller quenches it becomes larger due to the smaller energy difference between the pre and post-quench states, and the system can not equilibrate fast. Furthermore, the rapid small amplitude oscillations during the decay are a consequence of the quantum interference and are predominantly due to the overbarrier transport induced by the quench. Thus, they are also a presignature of the cradle mode which is discussed below. The fact that at least some frequencies of the cradle mode could be indirectly observed in the fidelity spectrum is not surprising. Indeed, from the expansion of the fidelity (see eq.(8)) in terms of the number states it is obvious that when the contribution of the excited band states, that refer to the

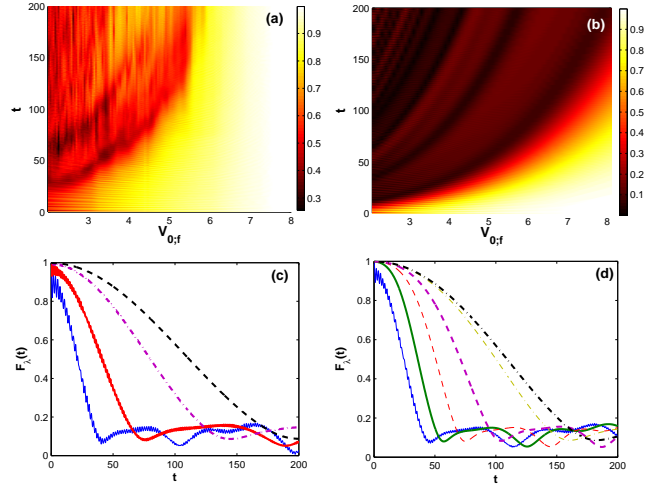


FIG. 10. (Color online) (a) Fidelity evolution as a function of different sudden negative quenches of the optical lattice depth. The system consists of five strongly interacting bosons ( $g = 5.0$ ) in an eight-well potential with  $V_{0;in} = 8.0$ . (b) Same but for different quenches of the lattice depth and a simultaneous interaction quench to  $g_f = 0.02$ . (c) Profiles of the fidelity evolution for different quench amplitudes  $\delta V_0 = -3.8$  (blue thin solid),  $\delta V_0 = -2.5$  (red thick solid),  $\delta V_0 = -0.9$  (magenta dashed-dotted),  $\delta V_0 = -0.2$  (black dashed) and a simultaneous interaction quench to  $g_f = 0.02$ . In (d) we present profiles of the fidelity following a negative time-dependent quench of the potential depth to  $V_{0,f} = 4.0$  with different ramp-rates  $\tau = 0.4\tau_H$  (blue thin solid),  $\tau = 15.0\tau_H$  (green thick solid),  $\tau = 40.0\tau_H$  (red thin dashed),  $\tau = 100.0\tau_H$  (magenta thick dashed),  $\tau = 400.0\tau_H$  (yellow thin dashed-dotted) and  $\tau = 800.0\tau_H$  (black thick dashed-dotted) and a simultaneous interaction quench to  $g_f = 0.02$ .

cradle, is significant the mode should also be observed in the fidelity spectrum. For smaller quenches these amplitude oscillations fade out, thereby indicating that the cradle is very weak.

Furthermore, in order to unravel the crossover between a diabatic and an adiabatic quench, let us consider a time-dependent scenario of the form  $V(t; \tau) = V_{0;in} + (V_{0,f} - V_{0;in}) \tanh(t/\tau)$ . To obtain the physically relevant time-scales, let us rescale the time  $t$  in units of the quench characteristic time scale  $\tau_H(\delta V_0) \sim 1/\Delta\epsilon(\delta V_0)$ , where  $\Delta\epsilon = \epsilon(V_{0;in}; g_{in}) - \epsilon(V_{0,f}; g_f)$  is the energy difference between the pre-quenched and the post-quenched system. Figure 10(d) demonstrates the fidelity in the course of the dynamics for an interaction quench to  $g_f = 0.02$  and the same final potential depth  $V_{0,f} = 4.4$  ( $V_{in} = 8.0$ ) for different ramp rates  $\tau$ . A direct observation, here, is that the system has a similar quadratic response (for short-times) with respect to the quench, being accompanied by small amplitude oscillations especially for fast quenches,  $\tau < 28\tau_H$ . This indicates that the characteristics of the dynamics, such as the excitation modes, remain also for finite rates. By considering large rates  $\tau$  the switch-on of the energy difference is

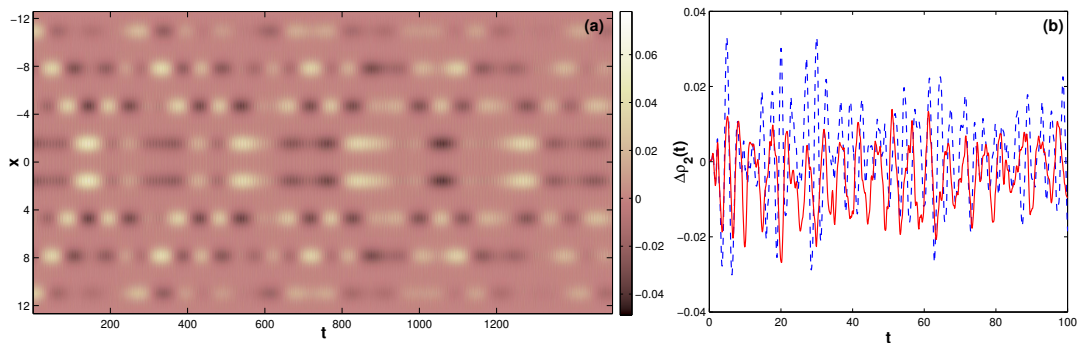


FIG. 11. (Color online) (a) The fluctuations  $\delta\rho(x, t)$  of the one-body density, for an eight-well setup with  $N = 5$ , caused by a sudden negative barrier quench from  $V_{0;in} = 8.0$  to  $V_{0;f} = 4.0$  and a simultaneous interaction quench from  $g_{in} = 5.0$  to  $g_f = 0.02$ . (b) The intrawell asymmetry  $\Delta\rho_2(t)$  for the second well of the eight well setup for a barrier quench (red solid curve) to  $V_{0;f} = 4.0$  and for the combined quench scenario, i.e. barrier and interaction quench, with final parameters  $V_{0;f} = 4.0$  and  $g_f = 0.02$  (blue dashed curve).

sufficiently slow and an eigenstate of the initial Hamiltonian becomes approximately an eigenstate for the instantaneous final Hamiltonian. In this manner, we tend to approach the adiabatic limit and the system equilibrates in a slower manner while the small amplitude fast oscillations tend to disappear. Note that for smaller relative quench amplitudes the adiabatic limit is attained for smaller ramp-rates due to the reduced impact of the quench.

The reduction of the lattice depth allows for an initially delocalized boson to overcome the barrier if its kinetic energy dominates with respect to the potential energy. Then, it is possible to perform a collision with a second particle on the neighboring site and a cradle state can be generated. Figure 11(a) illustrates from the perspective of the relative density  $\delta\rho(x, t)$  the evolution of the system after a negative change of the lattice depth from  $V_{0;in} = 8.0$  to  $V_{0;f} = 4.0$  and a simultaneous interaction quench from  $g_{in} = 5.0$  to  $g_f = 0.02$ . The dynamics shows the propagation of interwell tunneling via the population transport along the lattice, following the evolution of the bright regions. The corresponding propagation velocity is smaller for a smaller quench of the barrier. Furthermore, locally we observe the emergence of the cradle mode for the inner-well dynamics as a consequence of the overbarrier transport. However, this mode is hardly visible in Figure 11(a) due to the presented long evolution time and possesses a small amplitude as we shall demonstrate below.

The cradle mode refers to the inner-well oscillations between at least two bosons in the same well. The dominant number states for such a process exemplified using the first well are  $|2, 0, 1, 1, 1, 0, \dots\rangle_0$  and  $|2, 0, 1, 1, 1, 0, \dots\rangle_1$ , with a straightforward extension for the remaining wells. To identify the presence of the cradle mode for the present setup we show in Figure 11(b) the intrawell asymmetry ( $\Delta\rho_\alpha(t)$ ), for the second well of the lattice, as a function of time, and two different quench scenarios, i.e.

an instantaneous ramp-down of the lattice depth (red solid curve) and its combination with a simultaneous interaction quench to  $g_f = 0.02$  (blue dashed curve). In the latter case the resulting amplitude is larger, which is due to the simultaneous interaction quench. For an incommensurate setup with filling  $\nu > 1$  this amplitude is even more larger as the initially delocalized particles, energetically close to the barrier, render the system sensitive even to a small perturbation.

#### IV. Conclusions and Outlook

We have investigated the quantum dynamics of strongly interacting bosons following a quench either to a weakly interacting final state or to a lattice with lowered barriers. The observed normal modes consist of the interwell tunneling, a local breathing and a cradle mode. Each of these modes have been explained in detail, among others, within the concept of multiband Wannier number states which capture the population of excited states. The dominant Fock space for each mode has been identified showing the inclusion of higher-band contributions. In this manner, conceptual differences concerning the ingredients of each mode as well as the corresponding excitation process in comparison with the case of positive interaction quenched [14] superfluids have been demonstrated.

The interwell tunneling refers mainly to a direct population transport among the individual wells. On the other hand, the local breathing mode refers to expansion and contraction dynamics of the bosons in an individual well. The cradle mode corresponds to a localized wavepacket oscillation. For the interaction quench scenario where we start from a strongly interacting state and quench back to weak-interactions it is shown that the generation of the cradle mode is due to the initial delocalization. Therefore it can be observed only for setups with filling  $\nu > 1$ ,

while for the case of  $\nu \leq 1$  it can be excited only with the aid of a barrier quench. This is a major difference in comparison to a positively interaction quenched superfluid where due to import of energy in the system we allow for the over-barrier transport independently of the filling factor. The fidelity function has been employed in order to investigate the response of the system and its long time evolution with respect to the quench amplitude, as well as to show the dynamical crossover from a sudden to an adiabatic parameter change. By considering time-dependent quenches, i.e. different quench rates, or the modulation of various potential parameters of the Hamiltonian we proposed scenarios to control the excited modes by manipulating their frequencies.

Our developed understanding of the excitation modes as well as the tunneling dynamics may pave the way to a control of the nonequilibrium dynamics of such strongly correlated systems. For instance, the finite ramp-rate of a time-dependent quench may allow for the control of the normal modes or the transport of a definite number of atoms. There are many ways to proceed in this direction. As an example we mention the non-equilibrium dynamics of mixtures of different bosonic species in order to unravel their excitation modes or to create schemes for selective transport of an individual bosonic component.

#### Appendix: The Computational Method, ML-MCTDHB

Our analysis has been performed via the Multi-Layer Multi Configuration Time-Dependent Hartree method for Bosons (ML-MCTDHB) [24, 25] which constitutes an ab-initio method for the stationary properties but in particular the non-equilibrium quantum dynamics of bosonic systems. For a single species it is identical to MCTDHB which has been established [26, 27, 47] and applied extensively [47–50].

The advantage of the MCTDH-type methods [51] in comparison to other exact computational methods is the representation of the wavefunction by a set of variationally optimal time-dependent orbitals. In turn, this implies the truncation of the total Hilbert space to an optimal one by employing a time-dependent moving basis in which the system can be instantaneously optimally represented by time-dependent Hartree products. The use of time-dependent orbitals is the key for the numerically exact treatment, i.e. we need a much smaller set of time-adaptive orbitals in order to achieve the same level of accuracy compared to the case of a static basis. To be self contained let us briefly introduce the basic concepts of the method and discuss how it can be adapted to our purposes.

The main underlying idea of the MCTDHB method is to solve the time-dependent Schrödinger equation  $(i\hbar\partial_t - H)\Psi(x, t) = 0$  as an initial value problem. The expansion of the many-body wavefunction which is a lin-

ear combination of time-dependent permanents reads

$$|\Psi(t)\rangle = \sum_{\vec{n}} C_{\vec{n}}(t) |n_1, n_2, \dots, n_M; t\rangle, \quad (14)$$

where  $M$  is the number of orbitals and the summation is over all possible combinations which retain the total number of bosons. The permanents in terms of the creation operators  $a_j^\dagger(t)$  for the  $j$ -th orbital  $\varphi_j(t)$  are given by

$$|n_1, n_2, \dots, n_M; t\rangle = \frac{1}{\sqrt{n_1!n_2!\dots n_M!}} (a_1^\dagger)^{n_1} (a_2^\dagger)^{n_2} \times \dots (a_M^\dagger)^{n_M} |vac\rangle, \quad (15)$$

which satisfy the standard bosonic commutation relations  $[a_i(t), a_j(t)] = \delta_{ij}$ , etc. To proceed further, i.e. to determine the time-dependent wave function  $|\Psi\rangle$  we have to find the equations of motion for the coefficients  $C_{\vec{n}}(t)$  and the orbitals (which are both time-dependent). For that purpose one can employ various schemes such as the Lagrangian, McLachlan [52] or the Dirac-Frenkel [53, 54] variational principle. Following the Dirac-Frenkel variational principle  $\langle \delta\Psi | i\partial_t - \hat{H} | \Psi \rangle = 0$  we can determine the time evolution of all the coefficients  $C_{\vec{n}}(t)$  in the ansatz (14) and the time dependence for the orbitals  $|\varphi_j\rangle$ . In this manner, we end up with a set of  $M$  non-linear integrodifferential equations of motion for the orbitals which are coupled to the  $\frac{(N+M-1)!}{N!(M-1)!}$  linear equations of motion for the coefficients. These equations are the well-known MCTDHB equations of motion [26, 27, 47, 55].

In terms of our implementation we have used a discrete variable representation for the orbitals and a sin-DVR which intrinsically introduces hard-wall boundaries at both ends of the potential (i.e. zero value of the wave function on the first and the last grid point). For the preparation of our initial state we rely on the so-called relaxation method in terms of which we can obtain the lowest eigenstates of the corresponding  $n$ -well setup. The key idea is to propagate some initial wave function  $\Psi^{(0)}$  by the non-unitary  $e^{-H\tau}$  (propagation in imaginary time). As  $\tau \rightarrow \infty$ , this exponentially damps out any contribution but that stemming from the ground state like  $e^{-E_m\tau}$ . In turn, we change either the initial interparticle interaction or the depth of the optical lattice abruptly or in a time-dependent manner in order to study the evolution of  $\Psi(x_1, x_2, \dots, x_N; t)$  in the  $n$ -well potential within MCTDHB. Finally, note that in order to ensure the convergence of our simulations, e.g for the triple well, we have used up to 11 single particle functions thereby observing a systematic convergence of our results for sufficiently large spatial grids. Another criterion for ensuring convergence is the population of the lowest occupied natural orbital which is kept for each case below 0.1%.



## Acknowledgments

S.M. would like to thank P. Giannakeas, C. Morfonios and M. Mark for fruitful discussions. S.M. also thanks the Hamburgisches Gesetz zur Förderung des wissenschaftlichen und künstlerischen Nachwuchses (Hmb-

NFG) for a PhD Scholarship. L.C. and P.S. gratefully acknowledge funding by the Deutsche Forschungsgemeinschaft (DFG) in the framework of the SFB 925 Light induced dynamics and control of correlated quantum systems.

- 
- [1] I. Bloch, J. Dalibard, and W. Zwerger, *Rev. Mod. Phys.*, **80**, 885 (2008).
  - [2] A. Polkovnikov, K. Sengupta, A. Silva, and M. Vengalattore, *Rev. Mod. Phys.*, **83**, 863 (2011).
  - [3] M. Weidemüller, A. Hemmerich, A. Görlitz, T. Esslinger, and T. W. Hänsch, *Phys. Rev. Lett.*, **75**, 4583 (1995).
  - [4] C. L. Hung, X. Zhang, L. C. Ha, S. K. Tung, N. Gemelke, and C. Chin, *New J. Phys.*, **13**, 075019 (2011).
  - [5] J. P. Ronzheimer, M. Schreiber, S. Braun, S. S. Hodgman, S. Langer, I. P. McCulloch, F. Heidrich-Meisner, I. Bloch, and U. Schneider, *Phys. Rev. Lett.*, **110**, 205301 (2013).
  - [6] M. Rigol, V. Dunjko, and M. Olshanii, *Nature*, **452**, 854-858 (2008).
  - [7] M. Cheneau, P. Barmettler, D. Poletti, M. Endres, P. Schau, T. Fukuhara, C. Gross, I. Bloch, C. Kollath, and S. Kuhr, *Nature*, **481** no. 7382 484-487 (2012).
  - [8] S.S. Natu, and E. J. Mueller, *Phys. Rev. A*, **87**, 053607 (2013).
  - [9] E. Altman, and A. Auerbach, *Phys. Rev. Lett.*, **89**, 250404 (2002).
  - [10] D. Chen, M. White, C. Borries, and B. DeMarco, *Phys. Rev. Lett.*, **106**, 235304 (2011).
  - [11] H. Elmar, R. Hart, M. J. Mark, J. G. Danzl, L. Reichsöllner, M. Gustavsson, M. Dalmonte, G. Pupillo, and H.-C. Nägerl, *Nature*, **466** no. 7306: 597-600 (2010).
  - [12] K. W. Mahmud, L. Jiang, P. R. Johnson, and E. Tiesinga, *New J. Phys.* **16** 103009 (2014).
  - [13] S. Campbell, M. A. Garca-March, T. Fogarty, and T. Busch, *Phys. Rev. A* **90**, 013617 (2014).
  - [14] S. I. Mistakidis, L. Cao, and P. Schmelcher, *J. Phys. B: At. Mol. Opt. Phys.* **47** 225303 (2014).
  - [15] W. Kohn, *Phys. Rev.* **123**, 1242 (1961).
  - [16] M. Bonitz, K. Balzer, and R. Van Leeuwen, *Phys. Rev. B*, **76**, 045341 (2007).
  - [17] J. W. Abraham, and M. Bonitz, *Contributions to Plasma Physics*, **54**, 27-99 (2014).
  - [18] S. Bauch, K. Balzer, C. Henning, and M. Bonitz, *Phys. Rev. B*, **80**, 054515 (2009).
  - [19] S. Bauch, D. Hochstuhl, K. Balzer, and M. Bonitz, In *Journal of Physics: Conference Series* (Vol. **220**, No. 1, p. 012013). IOP Publishing (2010).
  - [20] J. W. Abraham, K. Balzer, D. Hochstuhl, and M. Bonitz, *Phys. Rev. B*, **86**, 125112 (2012).
  - [21] R. Schmitz, S. Krönke, L. Cao, and P. Schmelcher, *Phys. Rev. A*, **88**, 043601 (2013).
  - [22] S. Peotta, D. Rossini, M. Polini, F. Minardi, and R. Fazio, *Phys. Rev. Lett.*, **110**, 015302 (2013).
  - [23] P. Makotyn, C. E. Klauss, D. L. Goldberger, E. A. Cornell, and D. S. Jin, *Nature Phys.*, **9**, 512 (2014).
  - [24] L. Cao, S. Krönke, O. Vendrell, and P. Schmelcher, *J. Chem. Phys.*, **139**, 134103 (2013).
  - [25] S. Krönke, L. Cao, O. Vendrell, and P. Schmelcher, *New J. Phys.*, **15**, 063018 (2013).
  - [26] O. E. Alon, A. I. Streltsov, and L. S. Cederbaum, *J. Chem. Phys.*, **127**, 154103 (2007).
  - [27] O. E. Alon, A. I. Streltsov, and L. S. Cederbaum, *Phys. Rev. A*, **77**, 033613 (2008).
  - [28] M. Olshanii, *Phys. Rev. Lett.*, **81**, 938 (1998).
  - [29] R. Grimm, M. Weidemüller, and Y. B. Ovchinnikov, *Adv. At. Mol. Opt. Phys.*, **42**, 95-170 (2000).
  - [30] R. A. Duine, and H. T. Stoof, *Phys. Rep.*, **396**, 115-195 (2004).
  - [31] C. Chin, R. Grimm, P. Julienne, and E. Tiesinga, *Rev. Mod. Phys.*, **82**, 1225 (2010).
  - [32] J. I. Kim, V. S. Melezhik, and P. Schmelcher, *Phys. Rev. Lett.*, **97**, 193203 (2006).
  - [33] P. Giannakeas, F. K. Diakonov, and P. Schmelcher, *Phys. Rev. A*, **86**, 042703 (2012).
  - [34] T. Gorin, T. Prosen, T. H. Seligman, and M. Žnidarič, *Phys. Rep.*, **435**, 33-156 (2006).
  - [35] R. W. Spekkens, and J. E. Sipe, *Phys. Rev. A*, **59**, 3868 (1999).
  - [36] S. Klaiman, N. Moiseyev, and L. S. Cederbaum, *Phys. Rev. A*, **73**, 013622 (2006).
  - [37] E. J. Mueller, T. L. Ho, M. Ueda, and G. Baym, *Phys. Rev. A*, **74**, 33612 (2006).
  - [38] O. Penrose, and L. Onsager, *Phys. Rev.*, **104**, 576 (1956).
  - [39] M. P. Fisher, P. B. Weichman, G. Grinstein, and D. S. Fisher, *Phys. Rev. B*, **40**, 546 (1989).
  - [40] J. K. Freericks, and H. Monien, *EPL*, **26**, 545 (1994).
  - [41] J. K. Freericks, and H. Monien, *Phys. Rev. B*, **53**, 2691 (1996).
  - [42] K. Sakmann, A. I. Streltsov, O. E. Alon, and L. S. Cederbaum, *Phys. Rev. A*, **89**, 23602 (2014).
  - [43] S. Bravyi, M. B. Hastings, and F. Verstraete, *Phys. Rev. Lett.*, **97**, 050401 (2006).
  - [44] K. Sakmann, A. I. Streltsov, O. E. Alon, , and L. S. Cederbaum, *Phys. Rev. A*, **78**, 023615 (2008).
  - [45] I. Brouzos, S. Zöllner, and P. Schmelcher, *Phys. Rev. A*, **81**, 053613 (2010).
  - [46] A. Peres, *Am. J. Phys.*, **48**, 913 (1980).
  - [47] A. I. Streltsov, O. E. Alon, and L. S. Cederbaum, *Phys. Rev. Lett.*, **99**, 030402 (2007).
  - [48] A. I. Streltsov, K. Sakmann, O. E. Alon, and L. S. Cederbaum, *Phys. Rev. A*, **83**, 043604 (2011).
  - [49] O. E. Alon, A. I. Streltsov, and L. S. Cederbaum, *Phys. Rev. A*, **76**, 013611 (2007).
  - [50] O. E. Alon, A. I. Streltsov, and L. S. Cederbaum, *Phys. Rev. A*, **79**, 022503 (2009).
  - [51] M. H. Beck, A. Jäckle, G. A. Worth, and H. D. Meyer, *Phys. Rep.*, **324** (1999).
  - [52] A. D. McLachlan, *Mol. Phys.*, **8**, 39-44 (1964).
  - [53] J. Frenkel, *Wave mechanics*, (pp. 423-28). Oxford (1934).



- [54] P. A. Dirac, (1930, July). Proc. Camb. Phil. Soc. (Vol. **26**, No. 03, pp. 376-385). Cambridge University Press.
- [55] J. Broeckhove, L. Lathouwers, E. Kesteloot, and Van Leuven, P. Chem. Phys. Lett., **149**, 547-550 (1988).